Journal of Advanced Ceramics
2023, **12**(5): 1033–1045
https://doi.org/10.26599/JAC.2023.9220736
ISSN 2226-4108
CN 10-1154/TQ

Research Article

Xenotime-type high-entropy $(Dy_{1/7}Ho_{1/7}Er_{1/7}Tm_{1/7}Yb_{1/7}Lu_{1/7}Y_{1/7})PO_4$: A promising thermal/environmental barrier coating material for SiC_f/SiC ceramic matrix composites

Peixiong Zhang[a], Xingjun Duan[a], Xiaochang Xie[a], Donghai Ding[b], Tao Yang[a], Xinmei Hou[a,*], Yunsong Zhao[c,*], Enhui Wang[a,*]

[a]*Innovation Research Institute for Carbon Neutrality, University of Science and Technology Beijing, Beijing 100083, China*
[b]*College of Materials Science and Engineering, Xi'an University of Architecture and Technology, Xi'an 710055, China*
[c]*Science and Technology on Advanced High Temperature Structural Materials Laboratory, Beijing Institute of Aeronautical Materials, Beijing 100095, China*

Received: December 7, 2022; Revised: February 20, 2023; Accepted: February 26, 2023

Abstract: Rare-earth phosphates ($REPO_4$) are regarded as one of the promising thermal/environmental barrier coating (T/EBC) materials for SiC_f/SiC ceramic matrix composites (SiC-CMCs) owing to their excellent resistance to water vapor and CaO–MgO–Al_2O_3–SiO_2 (CMAS). Nevertheless, a relatively high thermal conductivity (κ) of the $REPO_4$ becomes the bottleneck for their practical applications. In this work, novel xenotime-type high-entropy $(Dy_{1/7}Ho_{1/7}Er_{1/7}Tm_{1/7}Yb_{1/7}Lu_{1/7}Y_{1/7})PO_4$ (HE $(7RE_{1/7})PO_4$) has been designed and synthesized for the first time to solve this issue. HE $(7RE_{1/7})PO_4$ with a homogeneous rare-earth element distribution exhibits high thermal stability up to 1750 ℃ and good chemical compatibility with SiO_2 up to 1400 ℃. In addition, the thermal expansion coefficient (TEC) of HE $(7RE_{1/7})PO_4$ (5.96×10^{-6} ℃$^{-1}$ from room temperature (RT) to 900 ℃) is close to that of the SiC-CMCs. What is more, the thermal conductivities of HE $(7RE_{1/7})PO_4$ (from 4.38 W·m^{-1}·K^{-1} at 100 ℃ to 2.25 W·m^{-1}·K^{-1} at 1300 ℃) are significantly decreased compared to those of single-component $REPO_4$ with the minimum value ranging from 9.90 to 4.76 W·m^{-1}·K^{-1}. These results suggest that HE $(7RE_{1/7})PO_4$ has the potential to be applied as the T/EBC materials for the SiC-CMCs in the future.

Keywords: high-entropy ceramics (HECs); $(Dy_{1/7}Ho_{1/7}Er_{1/7}Tm_{1/7}Yb_{1/7}Lu_{1/7}Y_{1/7})PO_4$ ($(7RE_{1/7})PO_4$); thermal/environmental barrier coatings (T/EBCs); thermal expansion coefficient (TEC); thermal conductivity (κ)

* Corresponding authors.
E-mail: X. Hou, houxinmeiustb@ustb.edu.cn;
Y. Zhao, yunsongzhao@163.com;
E. Wang, wangenhui@ustb.edu.cn

1 Introduction

Benefiting from the combination of excellent properties including high strength, superior corrosion resistance, high-temperature resistance, and high toughness together with low density, SiC_f/SiC ceramic matrix composites (SiC-CMCs) have been regarded as the most promising thermal-part candidate to replace Ni-based superalloys for the future aero-engine application [1–4]. However, when served in a high-velocity combustion environment at high temperatures, the protective SiO_2 film on the SiC-CMCs will be degraded. This is owing to a simultaneous reaction with water vapor and a low-melting-point oxide mixture of CaO–MgO–Al_2O_3–SiO_2 (CMAS), which can result in the recession of the SiC-CMCs in a long-term process [5–9]. Therefore, there is an urgent demand for advanced thermal/environmental barrier coatings (T/EBCs) to increase high-temperature tolerance and service life of the SiC-CMCs in harsh working conditions [9–15].

Up to now, rare-earth silicates ($RE_2Si_2O_7$ or RE_2SiO_5) have been developed as the most advantageous third-generation T/EBCs. They display superior high-temperature durability and corrosion resistance in comparison to the first-generation mullite and yttria-stabilized zirconia and the second-generation ($(1-x)BaO{\cdot}xSrO{\cdot}Al_2O_3{\cdot}2SiO_2$, $0 \leqslant x \leqslant 1$) T/EBCs [12,14,16–18]. In addition, the rare-earth silicates possess the double advantage of chemical stability together with rather low thermal conductivities (κ) [7,19–22]. Nevertheless, they are still confronted with the issue of water vapor corrosion owing to the formation of volatile $Si(OH)_4$. In addition, it is difficult to obtain single-phase, dense, and crack-free rare-earth silicate T/EBCs using the conventional atmospheric plasma spraying (APS) method due to silica evaporation [23–27]. Meanwhile, the CMAS deposited on the surface of the rare-earth silicates can further react to form new phases possessing unfavorable properties such as high thermal expansion coefficients (TECs) and low mechanical strength. In this context, discovering new non-silicate T/EBCs with improved comprehensive properties is well concerned. Recently, xenotime-type rare-earth phosphates ($REPO_4$) have gained more attention because of their excellent resistance to the water vapor corrosion owing to the absence of Si–O bonds [28]. References [28–33] confirm that $REPO_4$ (YPO_4, $YbPO_4$, $LuPO_4$, $ErPO_4$, and $ScPO_4$) possesses excellent high-temperature phase stability and resistance to the CMAS. However, the relatively high thermal conductivity (9.50–12.02 $W{\cdot}m^{-1}{\cdot}K^{-1}$ at room temperature (RT)) is still a notable disadvantage of single-component $REPO_4$ for their T/EBC applications [23,28,34–36].

High-entropy ceramics (HECs) are drawing increasing attention owing to their excellent intriguing properties, such as high hardness, low thermal conductivity, slow grain growth rate, and good resistance to corrosion [20,37–40]. Especially benefiting from the enhanced phonon scattering due to lattice distortion, the HECs usually possess lower thermal conductivities compared to single-component compounds [13,41–45]. The representative study reported by Zhao *et al*. [46] demonstrated that high-entropy (HE) monazite-type $(La_{0.2}Ce_{0.2}Nd_{0.2}Sm_{0.2}Eu_{0.2})PO_4$ with a lower thermal conductivity exhibits a great potential for the T/EBC of Al_2O_{3f}/Al_2O_3 CMCs. This implies that an HE strategy is a feasible approach to reducing the thermal conductivity of the single-component $REPO_4$. Considering significantly different requirements for the Al_2O_{3f}/Al_2O_3 CMCs and SiC-CMCs, further investigations on the validity of the HE $REPO_4$ for the SiC-CMCs remains to be implemented.

In this work, novel xenotime-type high-entropy $(Dy_{1/7}Ho_{1/7}Er_{1/7}Tm_{1/7}Yb_{1/7}Lu_{1/7}Y_{1/7})PO_4$ (HE $(7RE_{1/7})PO_4$) powders and the corresponding bulk have been designed and synthesized by the co-precipitation and pressure-less calcination method. The main criteria to determine rare-earth element composition are crystal structures and atomic radii. Firstly, the corresponding $REPO_4$ of selected elements should crystallize in the same xenotime structure, possessing the TEC similar to those of SiC_f/SiC CMCs. Secondly, the selected elements are required to have a similar ionic radius. Based on these, the elements Dy, Ho, Er, Tm, Yb, Lu, Y, and Sc are identified as potential candidates for HE $(7RE_{1/7})PO_4$. Considering that the Sc element is much more expensive, Dy, Ho, Er, Tm, Yb, Lu, and Y elements are selected herein. Phase composition, mechanical and thermal properties, as well as chemical compatibility were comprehensively investigated using various techniques. The results indicate that HE $(7RE_{1/7})PO_4$ can be a promising T/EBC material for the SiC-CMCs.

2 Experimental

2.1 Preparation and characterization of HE $(7RE_{1/7})PO_4$

HE $(7RE_{1/7})PO_4$ powders were synthesized by the co-precipitation method, and a schematic diagram is shown in Fig. 1. Firstly, seven rare-earth nitrate ($RE(NO_3)_3{\cdot}6H_2O$) powders (99.9% purity, Shanghai Aladdin Biochemical Technology Co., Ltd., China) were mixed in an equal molar ratio, and then dissolved in distilled water to form clear solution, in which the solution concentration is 0.03 mol·L^{-1} for $RE(NO_3)_3{\cdot}6H_2O$. H_3PO_4 (analytical reagent (AR), 85 wt%, Sinopharm Chemical Reagent Beijing Co., Ltd., China) dissolved in distilled water with 0.03 mol·L^{-1} was slowly added into the above solution and stirred thoroughly to obtain precursors of HE $(7RE_{1/7})PO_4$. The molar ratio of P to RE total was controlled to be 1.1 ∶ 1. Subsequently, the mixture was centrifuged and washed with deionized water at 3500 r·min^{-1} for 10 min until the pH value reached 6.0 or higher after several times. The obtained precursor of the HE $(7RE_{1/7})PO_4$ powders was re-suspended in alcoholic solution, and then dried in an oven (DZF-6050-L, Shanghai Binglin Electronic Technology Co., Ltd., China) at 80 ℃ for 24 h. Finally, the HE $(7RE_{1/7})PO_4$ powders were synthesized by calcining the precipitate at 1300 ℃ for 2 h. Single-component $REPO_4$ powders herein were also synthesized using the same way with one kind of specific $RE(NO_3)_3{\cdot}6H_2O$ as raw materials. The resulting powders were ball milled in ethyl alcohol with zirconia balls for 5 h by a planetary ball mill (XQM-2, Changsha MITR Instrument and Equipment Co., Ltd., China), and the slurry was dried, and then filtered by 300-mesh sieves to obtain fine particles.

HE $(7RE_{1/7})PO_4$ bulk and single-component $REPO_4$ bulk were uniaxially compacted into cylinders (ϕ14 mm × 2 mm) at 200 MPa for 2 min and calcined at 1650 ℃ or 6 h in a muffle furnace (KSL-1800X, Zhengzhou Kejing Electric Furnace Co., Ltd., China). The bulk density (ρ) of the fired cylinder samples were tested through Archimedes method. The theoretical density (D) of HE $(7RE_{1/7})PO_4$ is calculated by Eq. (1), where the rare-earth elements were assumed to distribute in sublattice sites uniformly. In Eq. (1), M denotes the molar mass of the crystalline substance, N is the number of the molecules in the unit cell, V is the unit cell volume, and N_A represents Avogadro's constant.

$$D = \frac{NM}{N_A V} \tag{1}$$

Phase compositions of the samples were identified using an X-ray diffractometer (D/max-2400, Rigaku, Japan) with Cu Kα radiation performed from 10° to 60° at a scanning rate of 5 (°)·min^{-1}. Rietveld refinements of X-ray diffraction (XRD) were analyzed using the General Structural Analysis System (GSAS) program for lattice constant analysis. Microstructural characterization and element distribution analysis were characterized using a field-emission scanning electron microscope (FE-SEM; GeminiSEM 300, ZEISS, Germany) equipped with an energy-dispersive X-ray spectrometer (EDS; Ultim Max 170, Oxford Instrument Technology (Shanghai) Co., Ltd., UK) and a transmission electron microscope (TEM; Talos F200X, FEI, USA). A grain size distribution was analyzed using the ImageJ software (National Institutes of Health, USA), where at least 300 grains were counted. In view of a fracture surface, the synthesized HE $(7RE_{1/7})PO_4$ bulk

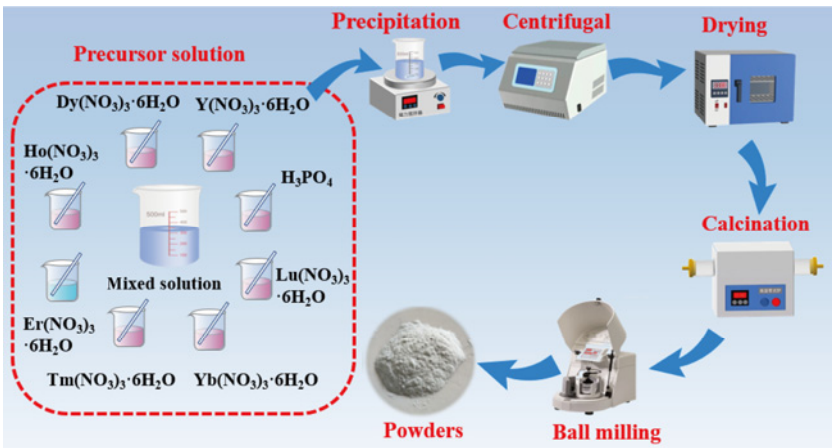

Fig. 1 Schematic diagram of preparation process of HE $(7RE_{1/7})PO_4$ powders.

was randomly broken into some small blocks using a hammer. A block with an appropriate size was then selected to observe with the aid of SEM analysis.

2.2 Mechanical properties of HE $(7RE_{1/7})PO_4$ bulk

A nanoindentation test was performed to measure nanohardness and reduced modulus using a nanoindenter (TMXP, MTS Systems Corp., USA) and a diamond Berkovich indenter (Guangzhou Zhi Cheng Technology Co., Ltd., China) with a tip radius of 20 nm [47]. During the test, the well-polished surface of the sample with a size of ϕ14 mm × 2 mm was performed at a space of 10 mm between the two adjacent points with a constant load of 8 mN held for 15 s.

2.3 Thermal properties of HE $(7RE_{1/7})PO_4$ bulk

The thermal conductivity was characterized by a laser flash analyzer (LFA457, NETZSCH, Germany) in an argon atmosphere within temperatures ranging from 100 to 1300 ℃ The HE $(7RE_{1/7})PO_4$ bulk with a size of ϕ12.7 mm × 2 mm was used and coated with platinum and graphite layers to prevent heat radiation.

The κ can be calculated from the heat capacity (c_p), ρ, and thermal diffusivity (D_{th}) by Eq. (2). Because the prepared bulks were not fully dense, the thermal conductivity (κ_0) of fully dense materials is corrected by Eq. (3) to exclude the influence of residual micropores. In Eq. (3), ϕ is the porosity that can be determined by the equation: $\phi = 1 - \rho/D$. Each measurement was repeated three times to acquire average values.

$$\kappa = D_{th} c_p \rho \tag{2}$$

$$\kappa_0 = \frac{\kappa}{1 - 3/2\phi} \tag{3}$$

The average TEC from RT to 900 ℃ in air was investigated via an optical dilatometer (DIL 402 Expedis Classic, NETZSCH, Germany). Testing bulks were rectangular bars with dimensions of 4 mm × 3 mm × 15 mm.

The high-temperature stability of HE $(7RE_{1/7})PO_4$ in the temperature ranging from RT to 1450 ℃ with a heating rate of 5 ℃·min^{-1} and argon flow of 25 mL·min^{-1} was identified by a thermogravimetric–differential thermal analyzer (STA 449 F1, NETZSCH, Germany). The phase stability was conducted via calcination at 1750 ℃ for 1 h, and was then evaluated by the XRD.

2.4 Chemical compatibility of HE $(7RE_{1/7})PO_4$

To characterize the chemical compatibility between HE $(7RE_{1/7})PO_4$ and SiO_2, the HE $(7RE_{1/7})PO_4$ powders and SiO_2 powders (SiO_2 ⩾ 99.9 wt%, Aladdin Biochemical Technology Co., Ltd., China) were mixed in an equal mass and milled by planetary ball-milling for 5 h in ethyl alcohol, and then dried in an oven. The mixed powders were compacted into cylinder shapes (ϕ12.7 mm × 5 mm) at a uniaxial pressure of 200 MPa, and then calcined in a furnace at 1400 ℃ for 5 h. After that, the calcined samples were crushed and ground into powders in an agate mortar. The phase compositions and microstructures of the mixed powders before and after annealing at 1400 ℃ were analyzed by the XRD and SEM.

3 Results and discussion

3.1 Phase compositions and microstructures of HE $(7RE_{1/7})PO_4$

3.1.1 HE $(7RE_{1/7})PO_4$ powders

Figures 2(a) and 2(b) present typical crystal structures of the single-component $REPO_4$ and HE $(7RE_{1/7})PO_4$, respectively. It can be seen that HE $(7RE_{1/7})PO_4$ has the same crystal structure as those of the single-component $REPO_4$, i.e., the tetragonal structure with the space group of $I4_1/amd$ ($Z = 4$ where Z is the number of molecules in the unit cell). As for HE $(7RE_{1/7})PO_4$, seven kinds of RE atoms occupy the RE sites randomly and form the tetragonal structure consisting of PO_4 tetrahedra and REO_8 dodecahedra [28,48]. The $REPO_4$ can be regarded as accumulating vertex- connected PO_4 tetrahedra and REO_8 dodecahedra. In the PO_4 tetrahedra, a P atom is surrounded by four O atoms. As for the REO_8 polyhedra, the RE atom is surrounded by eight O atoms. Each oxygen atom connects one P atom and two RE atoms, whereas each RE atom and P atom connect eight and four oxygen atoms, respectively.

Figure 2(c) shows XRD patterns of the synthesized HE $(7RE_{1/7})PO_4$ powders and the corresponding standard cards of the single-component $REPO_4$. It can be seen that the single phase of HE $(7RE_{1/7})PO_4$ without other impurities is synthesized. As displayed in Fig. 2(d) and Fig. S1 in the Electronic Supplementary Material (ESM), the characteristic peaks corresponding to the single-component $REPO_4$ shift toward higher

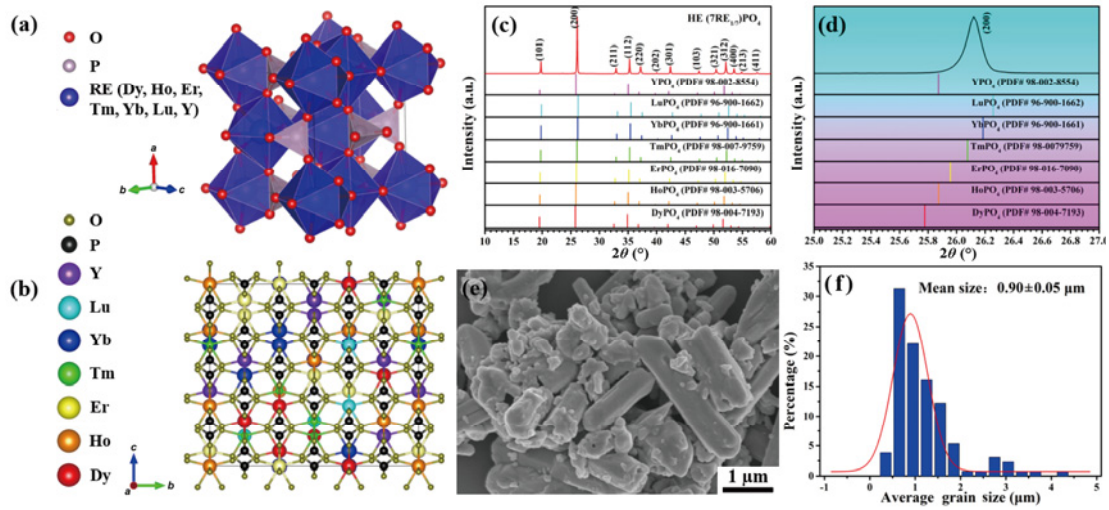

Fig. 2 Crystal structure patterns of (a) single-component $REPO_4$ and (b) HE $(7RE_{1/7})PO_4$; (c, d) XRD patterns, (e) SEM image, and (f) particle size distribution of HE $(7RE_{1/7})PO_4$ powders.

diffraction angles with the increase of RE^{3+} ionic radii. The highest diffraction peak (200) of HE $(7RE_{1/7})PO_4$ is lying in the middle position among these single-component $REPO_4$, suggesting that the lattice distortion is generated due to the equal proportional doping of multiple components in HE $(7RE_{1/7})PO_4$. Figure 2(e) shows that the morphologies of the HE $(7RE_{1/7})PO_4$ powders consist of two typical morphologies, i.e., irregular and rod-like grains. The size of the irregular grains is below 1 μm, while the rod-like grains exhibit a height of 1–3 μm and a diameter of less than 1 μm. The particle size distribution analysis (Fig. 2(f)) displays that the mean grain size of the HE $(7RE_{1/7})PO_4$ powders is 0.90±0.05 μm.

To obtain detailed information regarding lattice parameters of HE $(7RE_{1/7})PO_4$, Rietveld refinement is carried out, and the results are shown in Fig. 3. The values of fitting parameters consisting of R_p = 3.77% and R_{wp} = 5.83% (Fig. 3) suggest good reliability of Rietveld refinement where R_{wp} is the weighted sum of the squared differences between the observed and computed intensity values, and R_p is profile residual (unweighted). Table 1 summarizes the refined lattice parameters of HE $(7RE_{1/7})PO_4$ and other single-component $REPO_4$ obtained from JCPDS cards. Except for YPO_4, the lattice parameters of the single-component $REPO_4$ decrease continuously with the increasing atomic number of the rare-earth elements. The lattice parameters of HE $(7RE_{1/7})PO_4$ are calculated to be a = 6.8581 Å, b = 6.8581 Å, and c = 6.0064 Å, which are nearly equivalent to the average values of seven single-component $REPO_4$. Based on the above results, D of HE $(7RE_{1/7})PO_4$ is calculated to be 5.93 g·cm^{-3}.

To further clarify the crystal structures and elemental homogeneity of the HE $(7RE_{1/7})PO_4$ powders on the nanoscale, the TEM analysis is characterized, as shown in Fig. 4. In Figs. 4(a)–4(c), high-resolution TEM (HRTEM) and selected area electron diffraction (SAED)

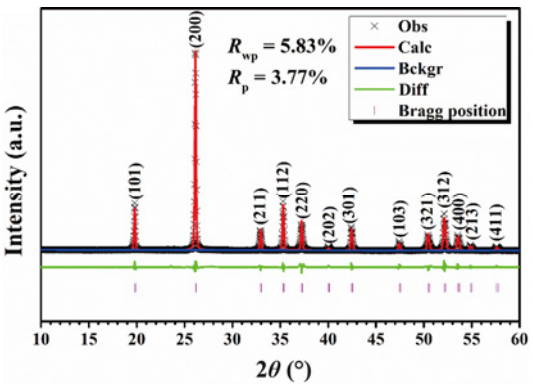

Fig. 3 XRD refinement pattern of HE $(7RE_{1/7})PO_4$ powders.

Table 1 Refined lattice parameters and corresponding *D* of HE $(7RE_{1/7})PO_4$ together with data of single-component $REPO_4$ obtained from JCPDS cards

Compound	a (Å)	b (Å)	c (Å)	D (g·cm^{-3})	JCPDS Card No.
YPO_4	6.8817	6.8817	6.0177	4.28	98-002-8554
$DyPO_4$	6.9070	6.9070	6.0460	5.93	98-004-7193
$HoPO_4$	6.8820	6.8820	6.0250	6.05	98-003-5706
$ErPO_4$	6.8600	6.8600	6.0030	6.21	98-016-7090
$TmPO_4$	6.8290	6.8290	5.9800	6.28	98-007-9759
$YbPO_4$	6.8010	6.8010	5.9650	6.44	96-900-1661
$LuPO_4$	6.7830	6.7830	5.9470	6.55	96-900-1662
HE $(7RE_{1/7})PO_4$	6.8581	6.8581	6.0064	5.93	—

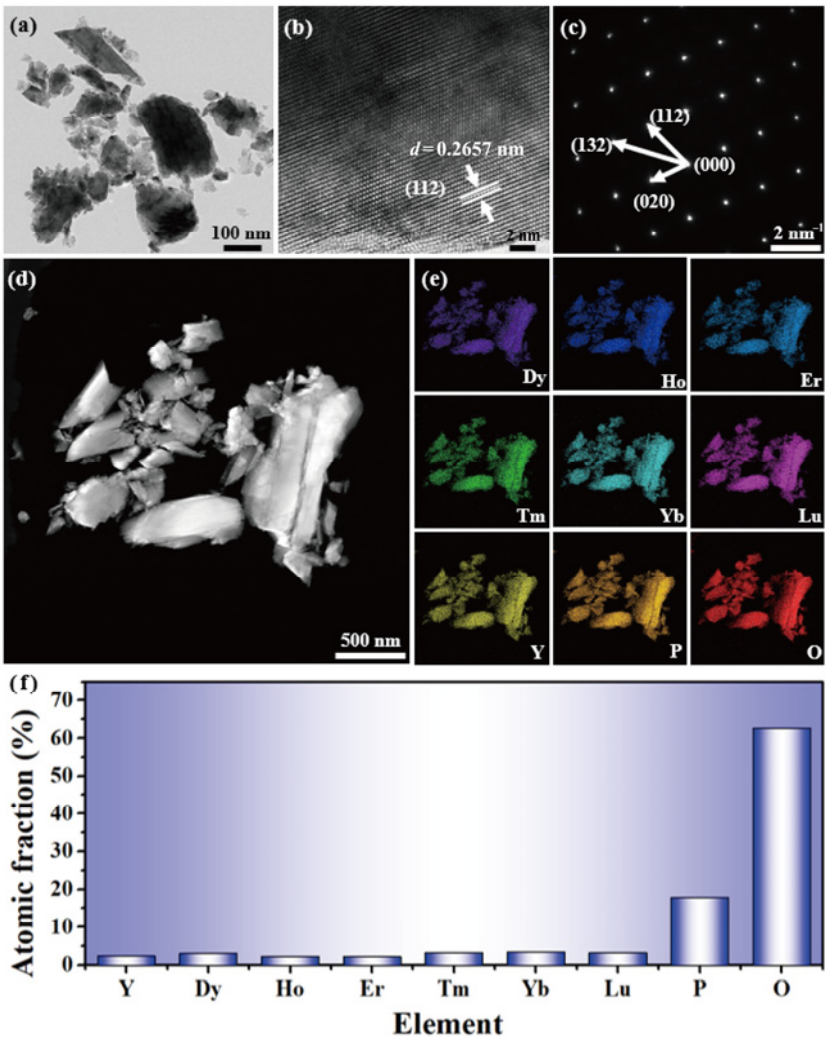

Fig. 4 TEM analysis of HE $(7RE_{1/7})PO_4$ powders: (a) TEM image, (b) HRTEM image, (c) SAED image, (d) high-angle annular dark field (HAADF) image, (e) EDS elemental mappings, and (f) atomic fractions of HE $(7RE_{1/7})PO_4$ powders.

images show that the HE $(7RE_{1/7})PO_4$ powders exhibit excellent crystallinity and sharp lattice fringes without defect, confirming the single phase of synthesized HE $(7RE_{1/7})PO_4$. Meanwhile, the measured interplanar spacing (d) is 0.2657 nm, corresponding to the d-spacing of the (112) plane of HE $(7RE_{1/7})PO_4$, which is consistent with the XRD results (Fig. 2(c)). Figures 4(d) and 4(e) display that the distribution of seven rare-earth elements within the grains are homogeneous with no element segregation according to energy-dispersive X-ray spectroscopy (EDS) elemental mappings. Atomic fractions (Fig. 4(f)) and X-ray fluorescence (XRF) characterization (Table S1 in the ESM) further verify that only single solid-solution phase is presented in the HE $(7RE_{1/7})PO_4$ powders with equimolar rare-earth elements.

3.1.2 HE $(7RE_{1/7})PO_4$ bulk

The phase compositions and microstructure analysis of the HE $(7RE_{1/7})PO_4$ bulk are carried out, as shown in Fig. 5. In Fig. 5(a), no impurity phase except HE $(7RE_{1/7})PO_4$ can be detected, indicating high phase purity of the HE $(7RE_{1/7})PO_4$ bulk. Figure 5(b) illustrates that the grains on the surface are nearly equiaxial, and the average grain size (the inset of Fig. 5(b)) is 5.24±0.17 μm. Compared with that of the HE $(7RE_{1/7})PO_4$ powders, the reason for the variation of grain morphology is inferred to be attributed to the space limitation on growth direction and welding effect of neighboring grains [49]. A similar behavior has been found in the morphological development of calcium hexaluminate [49,50]. The ρ of the HE $(7RE_{1/7})PO_4$ bulk is determined to be 5.57 $g \cdot cm^{-3}$. Combined with D of the HE $(7RE_{1/7})PO_4$ powders (Table 1), the relative density is calculated to be 93.93%, suggesting a relatively high density of the HE $(7RE_{1/7})PO_4$ bulk via the pressure-less calcination method. Figures 5(c)

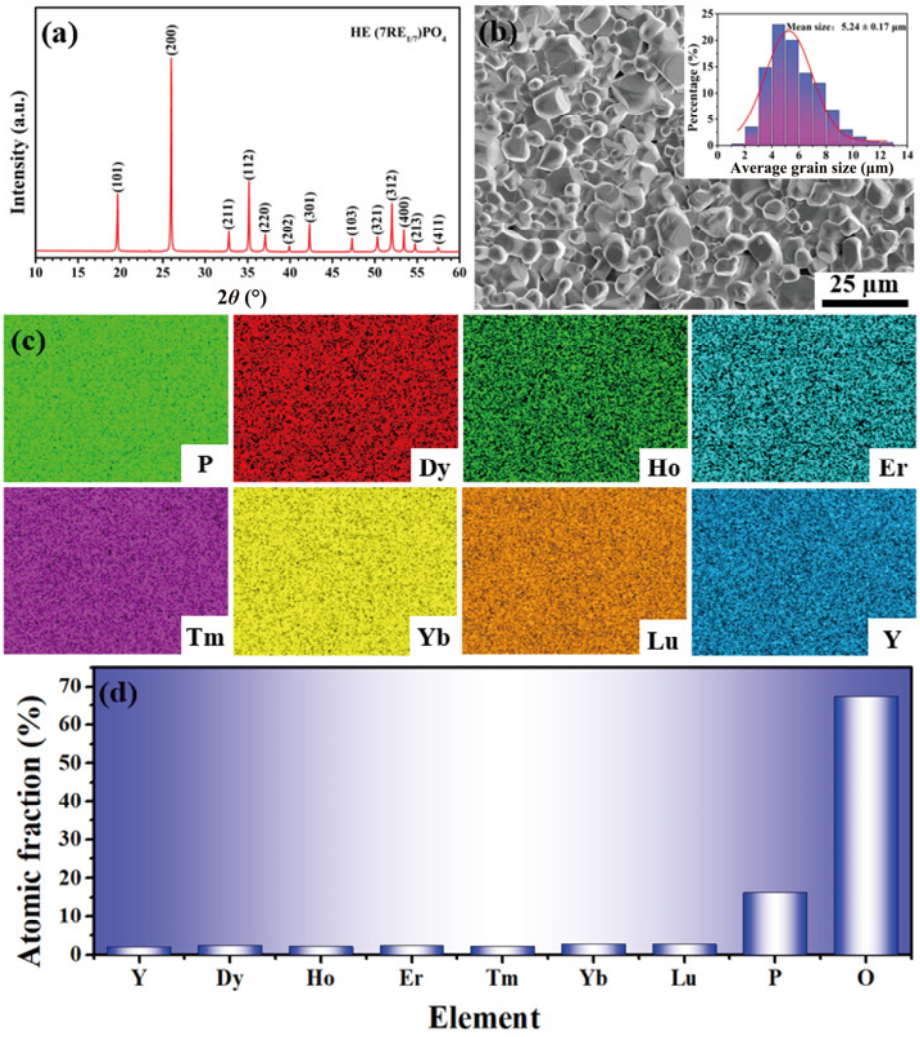

Fig. 5 (a) XRD pattern, (b) surface SEM image and particle size distribution, (c) EDS elemental mappings, and (d) atomic fractions of HE $(7RE_{1/7})PO_4$ bulk.

and 5(d) show that seven rare-earth elements exhibit a uniform distribution in the HE $(7RE_{1/7})PO_4$ bulk, which can verify high phase stability of the HE $(7RE_{1/7})PO_4$ powders during the calcination process.

3. 2 Mechanical properties of HE $(7RE_{1/7})PO_4$ bulk

Good mechanical properties and damage tolerance are basic requirements for the T/EBC materials. To evaluate the mechanical properties of the HE $(7RE_{1/7})PO_4$ bulk, the nanohardness and reduced modulus are measured with the single-component $REPO_4$ included for comparison, as listed in Table 2. In Table 2, the measured nanohardness value of the HE $(7RE_{1/7})PO_4$ bulk (10.42±0.81 GPa) is significantly higher than the "rule of mixture" value (7.48±1.11 GPa) from the average of the seven single-component $REPO_4$, which should be ascribed to solid-solution strengthening [49]. In view of the reduced modulus, the measured value of the HE $(7RE_{1/7})PO_4$ bulk

Table 2 Nanohardness, reduced moduli, and apparent porosity of HE $(7RE_{1/7})PO_4$ bulk and single-component $REPO_4$ bulks

Compound	Nanohardness (GPa)	Reduced modulus (GPa)	Apparent porosity (%)
$DyPO_4$	5.38±0.70	106.13±11.11	7.9
$HoPO_4$	6.29±1.27	132.30±9.11	6.15
$ErPO_4$	9.84±0.44	167.78±7.96	5.56
$TmPO_4$	8.65±1.19	180.86±8.55	6.65
$YbPO_4$	10.25±0.95	174.14±8.98	5.79
$LuPO_4$	7.99±1.94	136.76±9.17	6.75
YPO_4	3.93±1.25	97.26±28.17	8.58
Average value	7.48±1.11	142.17±11.86	—
HE $(7RE_{1/7})PO_4$	10.42±0.81	149.15±7.48	6.07

(149.15±7.48 GPa) is slightly higher than the "rule of mixture" value (142.17±11.86 GPa). By comparison, the reduced modulus of HE $(7RE_{1/7})PO_4$ is higher than those of $DyPO_4$, $HoPO_4$, $YbPO_4$, and $LuPO_4$ but is lower than those of $ErPO_4$, $TmPO_4$, and $YbPO_4$. This phenomenon may be caused by a combination of intrinsic quality and certain porosity of the corresponding bulks (Table 2). The similar results have been reported in HE $(Hf_{0.2}Zr_{0.2}Ta_{0.2}Nb_{0.2}Ti_{0.2})C$ [51], HE $(Y_{1/4}Ho_{1/4}Er_{1/4}Yb_{1/4})_2SiO_5$ [20], and medium-entropy $(Zr_{1/3}Nb_{1/3}Ti_{1/3})C$ [52].

Figure 6 illustrates a fracture surface of the HE $(7RE_{1/7})PO_4$ bulk after a fracture test at RT. It can be noticed that the fracture surface exhibits an intragranular fracture. The cleavage steps indicated by the white dotted box and river line patterns (RLPs) can be observed in the whole fracture surface, which is due to the cracks initiated from surface defects and extended inside the bulk. The formation of the cleavage steps is beneficial for promoting the dissipation of fracture energy, which is well associated with the relatively high nanohardness (Table 2).

3. 3 High-temperature stability of HE $(7RE_{1/7})PO_4$ bulk

High-temperature stability is a significant property to judge the reliability of the T/EBCs. To evaluate the high-temperature stability of the HE $(7RE_{1/7})PO_4$ bulk, both thermogravimetric–differential thermal analysis (TG–DTA) curves from RT to 1450 ℃ and calcination test at 1750 ℃ for 1 h are conducted, and the results are shown in Fig. 7. In Fig. 7(a), there is no apparent exothermic/endothermic peaks in the DTA curve and mass fluctuation in the TG curve, indicating that no decomposition or phase transition occurs during the non-isothermal process. The XRD pattern (Fig. 7(b)) displays that all the detected peaks can be indexed to the diffraction data of HE $(7RE_{1/7})PO_4$, which suggests that no polycrystalline transformation and new phases are formed during the calcination process. These results validate excellent high-temperature stability of the obtained HE $(7RE_{1/7})PO_4$ bulk.

3. 4 Chemical compatibility of HE $(7RE_{1/7})PO_4$

Chemical compatibility is a crucial requirement for the T/EBCs. The chemical compatibility of HE $(7RE_{1/7})PO_4$ with SiO_2 is investigated at 1400 ℃ for 5 h. Figure 8(a) displays the phase compositions of the HE $(7RE_{1/7})PO_4/SiO_2$ mixture before and after calcination. By comparison, it can be seen that no new phases besides the quartz crystallized from SiO_2 are generated in the HE $(7RE_{1/7})PO_4/SiO_2$ mixture. These results manifest that HE $(7RE_{1/7})PO_4$ possesses good chemical compatibility with SiO_2 during the calcination process. To further prove this, a HE $(7RE_{1/7})PO_4/SiO_2$ interface is analyzed, as presented in Fig. 8(b). It can be seen that dark gray-appearing phases of SiO_2 disperse

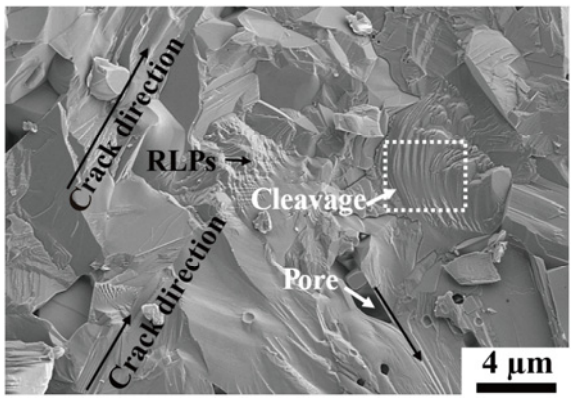

Fig. 6 Fracture surface of HE $(7RE_{1/7})PO_4$ bulk.

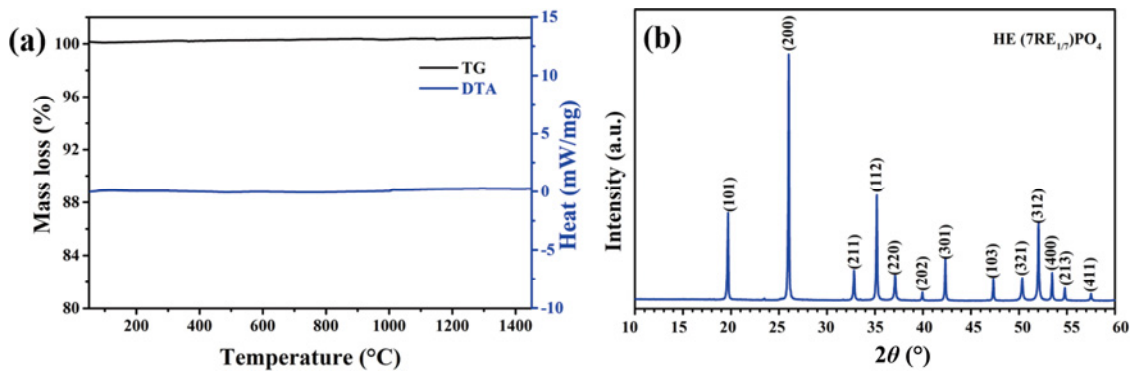

Fig. 7 (a) TG–DTA curves of HE $(7RE_{1/7})PO_4$ measured from RT to 1450 ℃ and (b) XRD patterns of the sample after calcination at 1750 ℃ for 1 h.

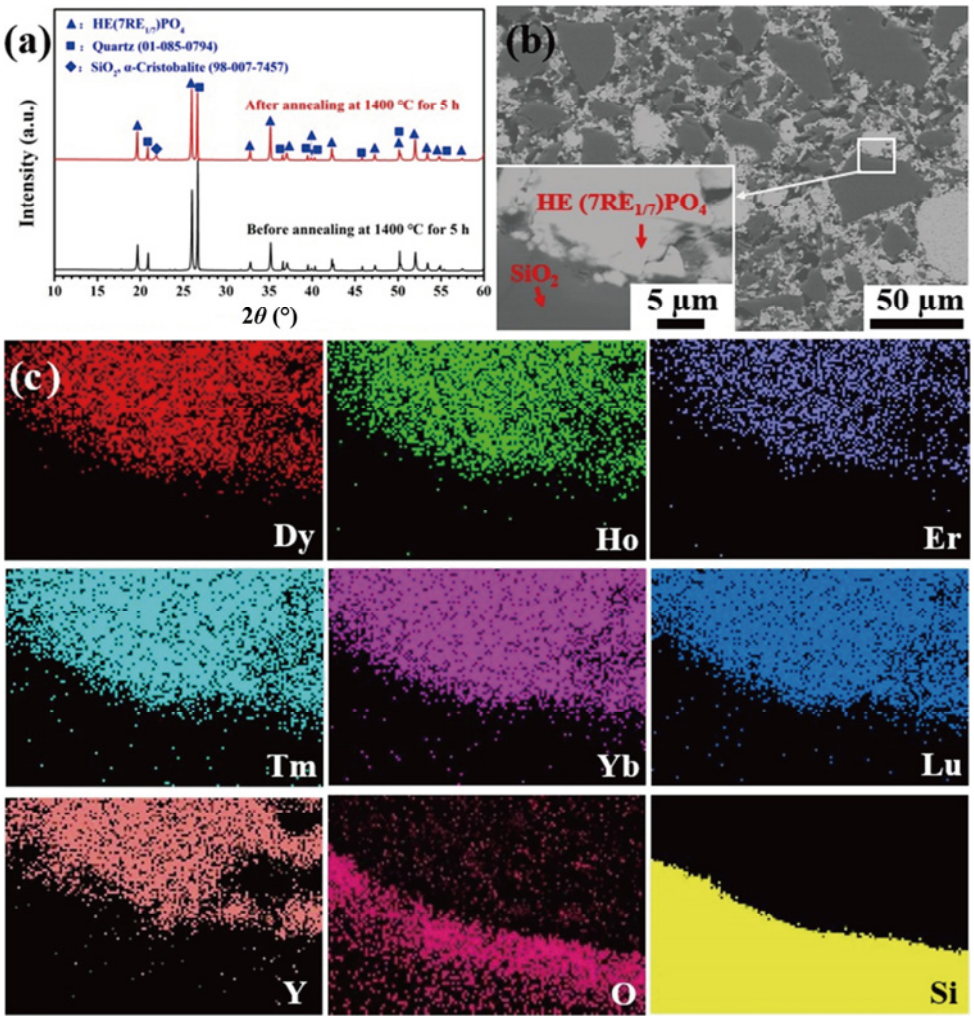

Fig. 8 (a) XRD patterns of HE $(7RE_{1/7})PO_4/SiO_2$ mixture before and after calcination at 1400 ℃ for 5 h, (b) backscattered electron (BSE) micrographs of HE $(7RE_{1/7})PO_4/SiO_2$ interface after calcination at 1400 ℃, and (c) corresponding EDS elemental mappings.

among bright white agglomerates of HE $(7RE_{1/7})PO_4$. The EDS elemental mappings (Fig. 8(c)) performed on this interface show that there is no element diffusion at the interface of the HE $(7RE_{1/7})PO_4/SiO_2$ mixture. The formation of two prominent black areas of circles in the EDS mapping of the element Y should be attributed to the difference in the depth of field, which may cause an error in the EDS analysis. This phenomenon also exists in other RE elements with different degrees. The above observations further confirm that the synthesized HE $(7RE_{1/7})PO_4$ can be compatible with the silicon oxide generated from the SiC-CMCs in the course of service.

3. 5 Thermal properties of HE $(7RE_{1/7})PO_4$ bulk

The thermal properties, including the thermal conductivity and TEC, are important parameters to determine the validity of the T/EBCs. Figure 9 plots the thermal conductivities of HE $(7RE_{1/7})PO_4$ and single-component $REPO_4$ measured from 100 to 1300 ℃. It can be seen that the changing trend for the HE $(7RE_{1/7})PO_4$ bulk is similar to that for the single-component $REPO_4$, i.e., the thermal conductivities monotonically decrease with the temperature. By comparison, the HE $(7RE_{1/7})PO_4$ bulk exhibits significantly lower thermal conductivities (from 4.38 $W \cdot m^{-1} \cdot K^{-1}$ at 100 ℃ to 2.25 $W \cdot m^{-1} \cdot K^{-1}$ at 1300 ℃) compared to all the single-component $REPO_4$. The lower thermal conductivity of the HE $(7RE_{1/7})PO_4$ bulk should be attributed to the lattice distortion and mass difference originating from multicomponent rare-earth doping. Based on this, the anharmonic phonon scattering is enhanced, and thus the lattice thermal conductivity is decreased by Eq. (4). Herein,

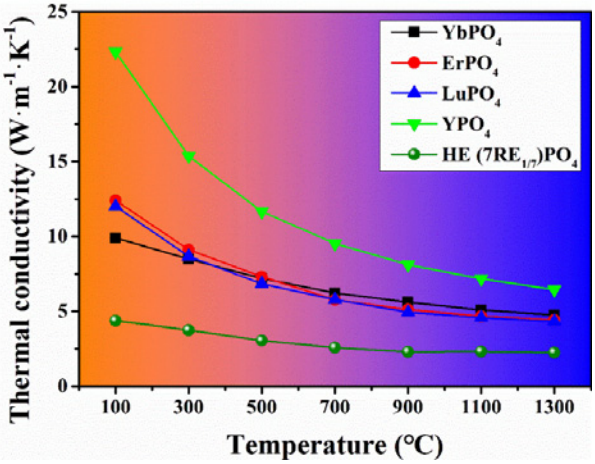

Fig. 9 Thermal conductivities of HE $(7RE_{1/7})PO_4$ bulk and single-component $REPO_4$ bulk [28] measured from 100 to 1300 ℃.

Γ_m, Γ_s, τ^{-1}, δ^3, v_m, and ω_D are the scattering parameters of mass fluctuation and strain field, thermal resistance, atomic volume, mean velocity, and Debye frequency, respectively [47,53].

$$\tau^{-1} = \frac{\delta^3 \omega_D^4}{4\pi v_m^4}(\Gamma_m + \Gamma_s) \quad (4)$$

The formation of HE $(7RE_{1/7})PO_4$ is a substitutional reaction among the seven single-component $REPO_4$. Those seven kinds of rare atoms are expected to occupy the RE sites randomly. Accordingly, numerous defects produced by substitutional atoms can be introduced into the lattices, which can increase the thermal resistance of HE $(7RE_{1/7})PO_4$. As we can see from Eq. (4), it is distinct that large-quantity mass and strain field fluctuations will be generated around substitutional atom defects, leading to the increase of Γ_m and Γ_s. This will in turn promote the thermal resistance and ultimately decrease the thermal conductivity of HE $(7RE_{1/7})PO_4$.

Figure 10 shows the TECs of HE $(7RE_{1/7})PO_4$ bulk measured between RT and 900 ℃. It can be seen that the expansion increases linearly with temperature without excessive fluctuation, indicating no occurrence of phase transition or decomposition. Table 3 summarizes the TECs of bulk HE $(7RE_{1/7})PO_4$ and single-component $REPO_4$ as well as the SiC-CMCs. It can be seen that the average TEC of HE $(7RE_{1/7})PO_4$ (5.97×10^{-6} ℃$^{-1}$) is slightly lower than those of the $REPO_4$, such as YPO_4 (6.2×10^{-6} ℃$^{-1}$), $HoPO_4$ (6.0×10^{-6} ℃$^{-1}$), $YbPO_4$ (6.0×10^{-6} ℃$^{-1}$), and $LuPO_4$ (6.2×10^{-6} ℃$^{-1}$) [36], but close to that of the

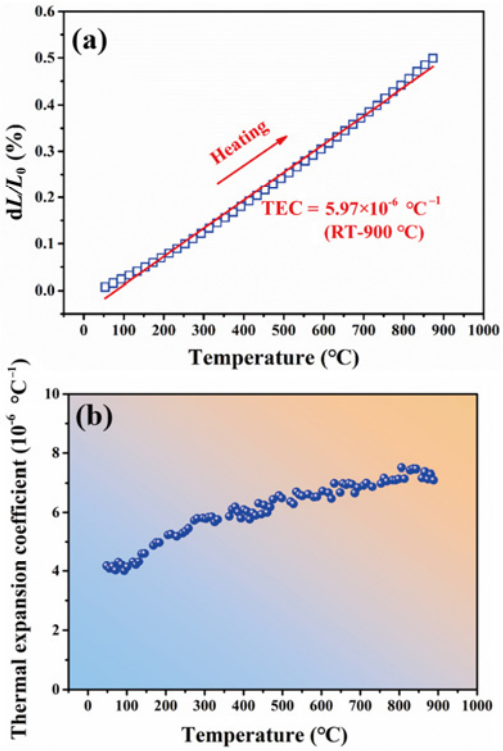

Fig. 10 (a) Linear thermal expansion curve and (b) TECs of HE $(7RE_{1/7})PO_4$ bulk measured between RT and 900 ℃ where L_0 is the length of the sample measured at room temperature, and dL is the difference between the length of the sample measured at different temperature and room temperature.

Table 3 TECs of HE $(7RE_{1/7})PO_4$ bulk and single-component $REPO_4$ bulks as well as SiC-CMCs at temperatures between RT and 900 ℃

Compound	TEC (10^{-6} ℃$^{-1}$)	Ref.
YPO_4	6.2	[36]
$DyPO_4$	—	—
$HoPO_4$	—	—
$ErPO_4$	6.0	[36]
$TmPO_4$	—	—
$YbPO_4$	6.0	[36]
$LuPO_4$	6.2	[36]
SiC-CMCs	4.5–5.5	[1,21,54]
HE $(7RE_{1/7})PO_4$	5.97	This work

SiC-CMCs ($(4.5–5.5)\times10^{-6}$ ℃$^{-1}$) [1,11,54]. Therefore, it is reasonable to conclude that HE $(7RE_{1/7})PO_4$ is a good match for the T/EBCs applied in the SiC-CMCs.

4 Conclusions

In this work, a novel HE $(7RE_{1/7})PO_4$ T/EBC material has been designed and synthesized for the SiC-CMCs

via the co-precipitation and pressure-less calcination method. This material has a tetragonal crystal structure with the space group of $I4_1/amd$ (Z = 4). Its nanohardness and reduced modulus are measured to be 10.42±0.81 and 149.15±7.48 GPa, respectively. In addition, HE $(7RE_{1/7})PO_4$ has good chemical compatibility with SiO_2 and thermal stability up to 1400 and 1750 ℃, respectively. The TEC of HE $(7RE_{1/7})PO_4$ from RT to 900 ℃ is 5.96×10^{-6} ℃$^{-1}$, which is close to that of the SiC-CMCs. It is worth highlighting that the thermal conductivities of HE $(7RE_{1/7})PO_4$ are from 4.38 W·m^{-1}·K^{-1} at 100 ℃ to 2.25 W·m^{-1}·K^{-1} at 1300 ℃, which are much lower than those of the single-component $REPO_4$. Therefore, HE $(7RE_{1/7})PO_4$ is a promising candidate for an available T/EBC material for the SiC-CMCs in the future.

Acknowledgements

This work was supported by the National Key R&D Program of China (No. 2021YFB3701404), the National Science Fund for Distinguished Young Scholars (No. 52025041), and the National Natural Science Foundation of China (Nos. 51904021 and 52174294).

Electronic Supplementary Material

Supplementary material is available in the online version of this article at https://doi.org/10.26599/JAC.2023.9220736.

References

[1] Lee KN, Fox DS, Bansal NP. Rare earth silicate environmental barrier coatings for SiC/SiC composites and Si_3N_4 ceramics. *J Eur Ceram Soc* 2005, **25**: 1705–1715.

[2] Klemm H. Silicon nitride for high-temperature applications. *J Am Ceram Soc* 2010, **93**: 1501–1522.

[3] Naslain R. Design, preparation and properties of non-oxide CMCs for application in engines and nuclear reactors: An overview. *Compos Sci Technol* 2004, **64**: 155–170.

[4] Zheng W, He XB, Wu M, *et al*. Graphite addition for SiC formation in diamond/SiC/Si composite preparation. *Int J Min Met Mater* 2019, **26**: 1166–1176.

[5] Hong ZL, Cheng LF, Zhang LT, *et al*. Water vapor corrosion behavior of scandium silicates at 1400 ℃. *J Am Ceram Soc* 2009, **92**: 193–196.

[6] Zhou YC, Zhao C, Wang F, *et al*. Theoretical prediction and experimental investigation on the thermal and mechanical properties of bulk β-$Yb_2Si_2O_7$. *J Am Ceram Soc* 2013, **96**: 3891–3900.

[7] Wang C, Liu M, Feng JL, *et al*. Water vapor corrosion behavior of Yb_2SiO_5 environmental barrier coatings prepared by plasma spray–physical vapor deposition. *Coatings* 2020, **10**: 392.

[8] More KL, Tortorelli PF, Walker LR, *et al*. High-temperature stability of SiC-based composites in high-water-vapor-pressure environments. *J Am Ceram Soc* 2003, **86**: 1272–1281.

[9] Wei ZY, Meng GH, Chen L, *et al*. Progress in ceramic materials and structure design toward advanced thermal barrier coatings. *J Adv Ceram* 2022, **11**: 985–1068.

[10] Xu J, Sarin VK, Dixit S, *et al*. Stability of interfaces in hybrid EBC/TBC coatings for Si-based ceramics in corrosive environments. *Int J Refract Met H* 2015, **49**: 339–349.

[11] Turcer LR, Padture NP. Towards multifunctional thermal environmental barrier coatings (TEBCs) based on rare-earth pyrosilicate solid-solution ceramics. *Scripta Mater* 2018, **154**: 111–117.

[12] Dong Y, Ren K, Lu YH, *et al*. High-entropy environmental barrier coating for the ceramic matrix composites. *J Eur Ceram Soc* 2019, **39**: 2574–2579.

[13] Zhao ZF, Chen H, Xiang HM, *et al*. High-entropy $(Y_{0.2}Nd_{0.2}Sm_{0.2}Eu_{0.2}Er_{0.2})AlO_3$: A promising thermal/environmental barrier material for oxide/oxide composites. *J Mater Sci Technol* 2020, **47**: 45–51.

[14] Tejero-Martin D, Bennett C, Hussain T. A review on environmental barrier coatings: History, current state of the art and future developments. *J Eur Ceram Soc* 2021, **41**: 1747–1768.

[15] Deng SJ, Wang P, He YD, *et al*. $La_2Zr_2O_7$ TBCs toughened by Pt particles prepared by cathode plasma electrolytic deposition. *Int J Min Met Mater* 2016, **23**: 704–715.

[16] Withey E, Petorak C, Trice R, *et al*. Design of 7 wt.% Y_2O_3–ZrO_2/mullite plasma-sprayed composite coatings for increased creep resistance. *J Eur Ceram Soc* 2007, **27**: 4675–4683.

[17] Cui YJ, Guo MQ, Wang CL, *et al*. Preparation and water–vapour corrosion behaviour of BSAS environmental barrier coatings fabricated on ceramic matrix composites. *Surf Coat Tech* 2022, **449**: 128953.

[18] Cojocaru CV, Lévesque D, Moreau C, *et al*. Performance of thermally sprayed Si/mullite/BSAS environmental barrier coatings exposed to thermal cycling in water vapor environment. *Surf Coat Tech* 2013, **216**: 215–223.

[19] Liu PP, Zhong X, Niu YR, *et al*. Reaction behaviors and mechanisms of tri-layer Yb_2SiO_5/$Yb_2Si_2O_7$/Si environmental barrier coatings with molten calcium–magnesium–alumino–silicate. *Corros Sci* 2022, **197**: 110069.

[20] Ren XM, Tian ZL, Zhang J, *et al*. Equiatomic quaternary $(Y_{1/4}Ho_{1/4}Er_{1/4}Yb_{1/4})_2SiO_5$ silicate: A perspective multifunctional thermal and environmental barrier coating material. *Scripta Mater* 2019, **168**: 47–50.

[21] Tian ZL, Zheng LY, Wang JM, *et al*. Theoretical and experimental determination of the major thermo-mechanical properties of RE_2SiO_5 (RE = Tb, Dy, Ho, Er, Tm, Yb, Lu, and Y) for environmental and thermal barrier coating applications. *J Eur Ceram Soc* 2016, **36**: 189–202.

[22] Wu Z, Sun LC, Tian ZL, *et al*. Preparation and properties of reticulated porous γ-$Y_2Si_2O_7$ ceramics with high porosity and relatively high strength. *Ceram Int* 2014, **40**: 10013–10020.

[23] Hu XX, Xu FF, Li KW, *et al*. Thermal properties and calcium–magnesium–alumina–silicate (CMAS) resistance of $LuPO_4$ as environmental barrier coatings. *J Eur Ceram Soc* 2020, **40**: 1471–1477.

[24] Zhu T, Niu YR, Zhong X, *et al*. Influence of phase composition on thermal aging behavior of plasma sprayed ytterbium silicate coatings. *Ceram Int* 2018, **44**: 17359–17368.

[25] Ueno S, Jayaseelan DD, Ohji T. Water vapor corrosion behavior of lutetium silicates at high temperature. *Ceram Int* 2006, **32**: 451–455.

[26] Ueno S, Jayaseelan DD, Ohji T, *et al*. Recession mechanism of $Lu_2Si_2O_7$ phase in high speed steam jet environment at high temperatures. *Ceram Int* 2006, **32**: 775–778.

[27] Ueno S, Ohji T, Lin HT. Recession behavior of $Yb_2Si_2O_7$ phase under high speed steam jet at high temperatures. *Corros Sci* 2008, **50**: 178–182.

[28] Han J, Wang YF, Liu RJ, *et al*. Theoretical and experimental investigation of xenotime-type rare earth phosphate $REPO_4$, (RE = Lu, Yb, Er, Y and Sc) for potential environmental barrier coating applications. *Sci Rep* 2020, **10**: 13681.

[29] Guo L, Zhang CL, He Q, *et al*. Corrosion products evolution and hot corrosion mechanisms of $REPO_4$ (RE = Gd, Nd, La) in the presence of V_2O_5+Na_2SO_4 molten salt. *J Eur Ceram Soc* 2019, **39**: 1496–1506.

[30] Wang F, Guo L, Wang CM, *et al*. Calcium–magnesium–alumina–silicate (CMAS) resistance characteristics of $LnPO_4$ (Ln = Nd, Sm, Gd) thermal barrier oxides. *J Eur Ceram Soc* 2017, **37**: 289–296.

[31] Boakye EE, Mogilevsky P, Parthasarathy TA, *et al*. Monazite coatings on SiC fibers I: Fiber strength and thermal stability. *J Am Ceram Soc* 2006, **89**: 3475–3480.

[32] Cinibulk MK, Fair GE, Kerans RJ. High-temperature stability of lanthanum orthophosphate (monazite) on silicon carbide at low oxygen partial pressures. *J Am Ceram Soc* 2008, **91**: 2290–2297.

[33] Hay RS, Mogilevsky P, Boakye E. Phase transformations in xenotime rare-earth orthophosphates. *Acta Mater* 2013, **61**: 6933–6947.

[34] Ji YQ, Marks NA, Bosbach D, *et al*. Elastic and thermal parameters of lanthanide-orthophosphate ($LnPO_4$) ceramics from atomistic simulations. *J Eur Ceram Soc* 2019, **39**: 4264–4274.

[35] Wang YG, Chen XH, Liu W, *et al*. Exploration of YPO_4 as a potential environmental barrier coating. *Ceram Int* 2010, **36**: 755–759.

[36] Hikichi Y, Ota T, Daimon K, *et al*. Thermal, mechanical, and chemical properties of sintered xenotime-type RPO_4 (R = Y, Er, Yb, or Lu). *J Am Ceram Soc* 1998, **81**: 2216–2218.

[37] Xue Y, Zhao XQ, An YL, *et al*. High-entropy $(La_{0.2}Nd_{0.2}Sm_{0.2}Eu_{0.2}Gd_{0.2})_2Ce_2O_7$: A potential thermal barrier material with improved thermo-physical properties. *J Adv Ceram* 2022, **11**: 615–628.

[38] Sun YN, Xiang HM, Dai FZ, *et al*. Preparation and properties of CMAS resistant bixbyite structured high-entropy oxides RE_2O_3 (RE = Sm, Eu, Er, Lu, Y, and Yb): Promising environmental barrier coating materials for Al_2O_3f/Al_2O_3 composites. *J Adv Ceram* 2021, **10**: 596–613.

[39] Dong Y, Ren K, Wang QK, *et al*. Interaction of multicomponent disilicate $(Yb_{0.2}Y_{0.2}Lu_{0.2}Sc_{0.2}Gd_{0.2})_2Si_2O_7$ with molten calcia–magnesia–aluminosilicate. *J Adv Ceram* 2022, **11**: 66–74.

[40] Xiang HM, Xing Y, Dai FZ, *et al*. High-entropy ceramics: Present status, challenges, and a look forward. *J Adv Ceram* 2021, **10**: 385–441.

[41] Liu DB, Wang YG, Zhou FF, *et al*. A novel high-entropy $(Sm_{0.2}Eu_{0.2}Tb_{0.2}Dy_{0.2}Lu_{0.2})_2Zr_2O_7$ ceramic aerogel with ultralow thermal conductivity. *Ceram Int* 2021, **47**: 29960–29968.

[42] Zhao ZF, Chen H, Xiang HM, *et al*. $(Y_{0.25}Yb_{0.25}Er_{0.25}Lu_{0.25})_2(Zr_{0.5}Hf_{0.5})_2O_7$: A defective fluorite structured high entropy ceramic with low thermal conductivity and close thermal expansion coefficient to Al_2O_3. *J Mater Sci Technol* 2020, **39**: 167–172.

[43] Zhao ZF, Xiang HM, Dai FZ, *et al*. $(La_{0.2}Ce_{0.2}Nd_{0.2}Sm_{0.2}Eu_{0.2})_2Zr_2O_7$: A novel high-entropy ceramic with low thermal conductivity and sluggish grain growth rate. *J Mater Sci Technol* 2019, **35**: 2647–2651.

[44] Chen H, Zhao ZF, Xiang HM, *et al*. High entropy $(Y_{0.2}Yb_{0.2}Lu_{0.2}Eu_{0.2}Er_{0.2})_3Al_5O_{12}$: A novel high temperature stable thermal barrier material. *J Mater Sci Technol* 2020, **48**: 57–62.

[45] Zhao ZF, Xiang HM, Chen H, *et al*. High-entropy $(Nd_{0.2}Sm_{0.2}Eu_{0.2}Y_{0.2}Yb_{0.2})_4Al_2O_9$ with good high temperature stability, low thermal conductivity, and anisotropic thermal expansivity. *J Adv Ceram* 2020, **9**: 595–605.

[46] Zhao ZF, Chen H, Xiang HM, *et al*. $(La_{0.2}Ce_{0.2}Nd_{0.2}Sm_{0.2}Eu_{0.2})PO_4$: A high-entropy rare-earth phosphate monazite ceramic with low thermal conductivity and good compatibility with Al_2O_3. *J Mater Sci Technol* 2019, **35**: 2892–2896.

[47] Ye BL, Wen TQ, Nguyen MC, *et al*. First-principles study, fabrication and characterization of $(Zr_{0.25}Nb_{0.25}Ti_{0.25}V_{0.25})C$ high-entropy ceramics. *Acta Mater* 2019, **170**: 15–23.

[48] Khadraoui Z, Bouzidi C, Horchani-Naifer K, *et al*. Crystal structure, energy band and optical properties of dysprosium monophosphate $DyPO_4$. *J Alloys Compd* 2014, **617**: 281–286.

[49] Domínguez C, Chevalier J, Torrecillas R, *et al*. Microstructure development in calcium hexaluminate. *J Eur Ceram Soc* 2001, **21**: 381–387.

[50] Domínguez C, Torrecillas R. Influence of Fe^{3+} on sintering and microstructural evolution of reaction sintered calcium hexaluminate. *J Eur Ceram Soc* 1998, **18**: 1373–1379.

[51] Ye BL, Wen TQ, Huang KH, *et al*. First-principles study, fabrication, and characterization of $(Hf_{0.2}Zr_{0.2}Ta_{0.2}Nb_{0.2}Ti_{0.2})C$ high-entropy ceramic. *J Am Ceram Soc* 2019, **102**: 4344–4352.
[52] Ye BL, Chu YH, Huang KH, *et al*. Synthesis and characterization of $(Zr_{1/3}Nb_{1/3}Ti_{1/3})C$ metal carbide solid-solution ceramic. *J Am Ceram Soc* 2018, **102**: 919–923.
[53] Li ML, Zhao XT, Shao G, *et al*. Oscillatory pressure sintering of high entropy $(Zr_{0.2}Ta_{0.2}Nb_{0.2}Hf_{0.2}Mo_{0.2})B_2$ ceramic. *Ceram Int* 2021, **47**: 8707–8710.
[54] Tian ZL, Zheng LY, Wang JY. Synthesis, mechanical and thermal properties of a damage tolerant ceramic: β-$Lu_2Si_2O_7$. *J Eur Ceram Soc* 2015, **35**: 3641–3650.